Cell-Membrane Coated Semiconducting Polymer Nanoparticles for Enhanced Multimodal Cancer Phototheranostics

*Jingchao Li, Xu Zhen, Yan Lyu, Yuyan Jiang, Jiaguo Huang, and Kanyi Pu**

School of Chemical and Biomedical Engineering, Nanyang Technological University, Singapore 637457, Singapore

ABSTRACT. Phototheranostic nanoagents are promising for early diagnosis and precision therapy of cancer. However, their imaging ability and therapeutic efficacy are often limited due to the presence of delivery barriers in tumor microenvironment. Herein, we report the development of organic multimodal phototheranostic nanoagents that can biomimetically target cancer-associated fibroblasts in tumor microenvironment for enhanced multimodal imaging-guided cancer therapy. Such biomimetic nanocamouflages comprise a near-infrared (NIR) absorbing semiconducting polymer nanoparticle (SPN) coated with the cell membranes of activated fibroblasts. The homologous targeting mechanism allows the activated fibroblast cell membrane coated SPN (AF-SPN) to specifically target cancer-associated fibroblasts, leading to enhanced tumor accumulation relative to the uncoated and cancer cell membrane coated counterparts after systemic administration in living mice. As such, AF-SPN not only provides stronger NIR fluorescence and photoacoustic (PA) signals to detect tumors, but also generates enhanced cytotoxic heat and single oxygen to exert combinational photothermal and photodynamic therapy, ultimately leading to an antitumor efficacy higher than the counterparts. This study thus introduces an organic phototheranostic system that biomimetically target the component in tumor microenvironment for enhanced multimodal cancer theranostics.

KEYWORDS: polymer nanoparticles, cell membrane, cancer phototherapy, photoacoustic imaging, phototheranostic agents

Theranostic nanoagents that integrate diagnostic and therapeutic components into a single entity allow to detect early-stage disease, evaluate the targeting of therapeutic agents, and monitor therapeutic responses in real time, providing opportunities for precision medicine.[1-4] In particular, phototheranostic nanoagents that utilize light irradiation to generate optical signals and phototherapeutic effects have attracted a great deal of attention,[5-8] mainly because of the simple maneuverability and high spatiotemporal resolution of light. However, similar to other nanoparticle-based drug delivery systems, conventional phototheranostic nanoagents generally encounter the issues of early recognition by the immune systems, fast clearance by the reticuloendothelial system (RES) and low accumulation at tumor site, which compromise their potential for clinical translation.[9] Although surface modification of phototheranostic nanoagents using synthetic polymers or targeting ligands can mitigate these problems, their effectiveness is still limited.[10-12]

Cell membrane coating has emerged as an effective biomimetic approach to camouflage the nanoparticles for optimized cancer therapy.[12-16] The adhesion proteins, antigens and membrane structure of source cell membranes can be reserved on the surface of cell membrane coated nanoparticles.[9] Thereby, cell membrane camouflaged nanoparticles can acquire related surface properties and functions of nature cell membranes. For example, with the intrinsic ability to enable immune evasion and prolonged blood circulation time, red blood cell membranes have been used to camouflage perfluorocarbon, polymeric, silica, magnetic and metal-organic framework (MOF) nanoparticles for imaging-guided cancer radiotherapy and chemotherapy.[17-21] Moreover, cancer cell membranes have been found to undergo a homologous binding process and thus used to enhance the targeting delivery of MOF, iron oxide and polymeric nanoparticles into tumors.[22-24] Similarly, other cell lines with tumor-homing capability such as platelets have

been used to coated iron oxide nanoparticles for magnetic resonance (MR) imaging guided cancer phototherapy.[25] However, only a few inorganic phototheranostic nanoparticles have been adopted this biomimetic approach for enhanced cancer therapy.[26]

Although improved chemotherapy efficacies have been achieved by cell membrane-camouflaged nanomedicines, effective transportation of nanoparticles into solid tumors is still challenged by the barriers in tumor microenvironment.[27-31] As a predominant population of tumor stromal cells in tumor microenvironment, cancer-associated fibroblasts are recognized as the key barriers for cancer therapy. On one hand, they secrete numerous growth factors and cytokines to activate correlative signaling pathways for promoting tumor initiation, angiogenesis, progression, metastasis and resistance. On the other hand, through surrounding tumor cells and producing extracellular matrix (ECM) components, cancer-associated fibroblasts construct a protecting physical barrier for tumor cells to impede the delivery of anti-cancer drugs and nanoparticles.[32] Studies have been proved that chemical modification of nanoparticles to target and kill cancer-associated fibroblasts have enabled depletion of tumor-stroma biological interactions and in turn led to enhanced chemotherapy.[33] However, the cell membranes of fibroblasts have not been utilized to camouflage nanoparticles for cancer theranostics.

As an emerging category of organic photonic nanoparticles, semiconducting polymer nanoparticles (SPNs) have gained increasing attention due to their excellent optical properties and good biocompatibility.[34-38] In particular, the structural versatility of SPNs allows them to be applied for near-infrared (NIR) fluorescence,[39] chemiluminescence,[40] photoacoustic (PA),[41-43] afterglow imaging,[44] and phototherapy,[45-47] as well as for remote photoactivation of enzymatic activity,[48] ion channels,[49] and gene expression.[38, 50] In this study, we report the development of biomimetic SPNs camouflaged with activated fibroblast (AF) cell membranes for enhanced

multimodal cancer phototheranostics. Such an organic nanocamouflage, termed as AF-SPN, comprises a highly NIR absorbing semiconducting polymer (SP), poly(cyclopentadithiophene-alt-benzothiadiazole) (PCPDTBT) (Figure 1a) and AF cell membrane as the core and shell, respectively. The SP servers as the theranostic agent to generate not only NIR fluorescence and PA signals for imaging but also single oxygen ($^1O_2$) and heat for combined photodynamic and photothermal therapy. The surface coated AF cell membranes render the homologous targeting towards cancer-associated fibroblasts (Figure 1b), promoting nanoparticle accumulation in tumors and consequently enhancing photodiagnostic and phototherapeutic efficacies (Figure 1c). In the following, we first describe the synthesis and characterization of AF-SPN along with the control nanoparticles including the uncoated SPN (uSPN) and the cancer-cell-membrane coated SPN (CC-SPN). Then, we study the homologous targeting abilities of these SPNs toward AF cells and cancer cells *in vitro*. At last, the proof-of-concept application of AF-SPN as a highly effective phototheranostic nanoagent is demonstrated and compared with CC-SPN in a tumor xenograft mouse model.

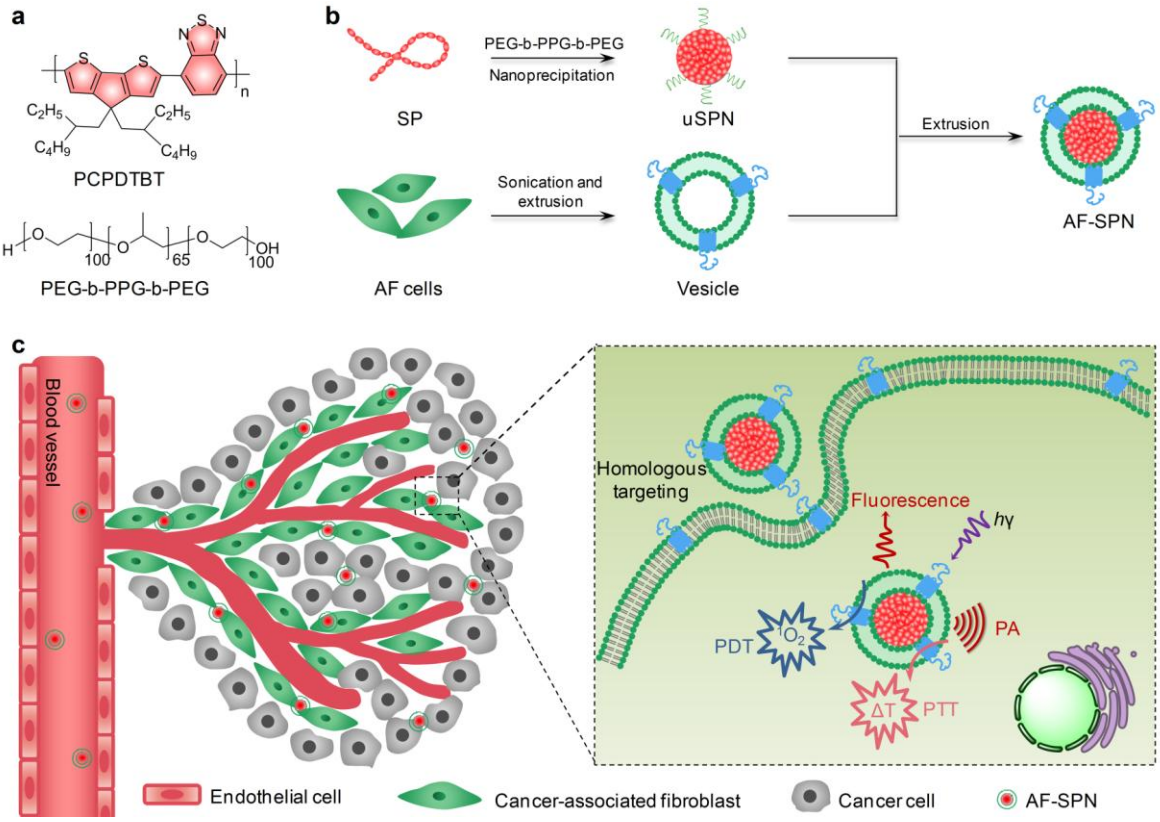

Figure 1. Schematic illustration of the preparation of AF-SPN for enhanced multimodal cancer phototheranostics. (a) Chemical structures of PCPDTBT and PEG-b-PPG-b-PEG used for preparation of SPNs. (b) Preparation procedure of AF-SPN. (c) Schematic illustration of the homologous targeting of AF-SPN to cancer-associated fibroblasts in tumor tissues for enhanced multimodal cancer phototheranostics.

RESULTS AND DISCUSSION

The development of AF-SPN consisted of the following three steps (Figure 1b): synthesis of the uncoated SPNs (uSPN), preparation of AF-derived vesicles and coating of AF-derived vesicles onto the surface of uSPNs. PCPDTBT was transformed into uSPN through nano-precipitation with the assistance of an amphiphilic triblock copolymer, poly(ethylene glycol)-block-poly(propylene glycol)-block-poly(ethylene glycol) (PEG-b-PPG-b-PEG, Figure 1a). To yield AF-derived vesicles, normal fibroblasts were first stimulated by transforming growth factor

(TGF-β1) for 2 days to induce them into AF cells with a high expression of fibroblast activation protein-alpha (FAP-α);[51] the obtained AF cells were then sonicated and extruded through 400 nm polycarbonate porous membranes. To coat AF cell membrane onto the surface of uSPN, freshly prepared AF-derived vesicles were co-extruded with uSPN through 100 nm polycarbonate porous membranes. 4T1 cancer cell membrane coated SPNs (CC-SPN) were prepared in a similar way and used as a control.

The physicochemical characterizations of SPNs before and after cell membrane coatings were studied. In contrast to uSPN (Figure 2a), both CC-SPN and AF-SPN showed an obvious core/shell structure and the outer shell was ~10 nm in thickness (Figure 2b,c). Agarose gel electrophoresis was used to confirm the size changes after cell membrane coatings as larger nanoparticles migrated slower.[49] With the cell membrane shell, both CC-SPN and AF-SPN migrated less than uSPN in the agarose gel electrophoresis (Figure 2d). The diameter was significantly increased from 30 nm for uSPN to 47 nm for both CC-SPN and AF-SPN (Figure 2e). Meanwhile, the zeta potentials of CC-SPN and AF-SPN were measured to be -19.1 and -20.0 mV, respectively (Figure 2f), similar to their source cell membrane derived vesicles (-21.1 mV for CC-derived vesicles and -22.6 mV for AF-derived vesicles), but significantly lower than that of uSPN (-9.5 mV). To further confirm the coatings of cell membrane, a fluorescent lipophilic membrane dye, 3-octadecyl-2-[3-(3-octadecyl-2(3H)-benzoxazolylidene)-1-propenyl]-perchlorate (Dio), was used to label the cell membrane, whose fluorescence could be turned on in the bilayer lipid structure.[52] Both CC-SPN and AF-SPN showed obvious fluorescence signals of Dio at 501 nm, while fluorescence signal was barely detectable for uSPN (Figure S1, Supporting Information). All of these results confirmed that the cell membranes derived from AF cells or cancer cells were coated onto the surface of SPNs. The protein contents in CC-SPN and

AF-SPN were investigated by sodium dodecyl sulfate-polyacrylamide gel electrophoresis (SDS-PAGE), showing that almost all cell membrane proteins were extensively retained on the surface of nanoparticles (Figure S2, Supporting Information). In addition, the diameters of uSPN, CC-SPN and AF-SPN did not have any obvious changes after 15 days of storage in phosphate buffered saline (PBS) buffer (Figure S3, Supporting Information), indicating their good colloidal stability.

Influence of cell membrane coatings on the optical, photothermal and photodynamic properties of SPNs was studied. As compared to uSPN, the characteristic absorption peaks of PCPDTBT at 407 and 670 nm remained nearly unchanged for both nanocamouflages (CC-SPN and AF-SPN) (Figure 2g). In addition, uSPN, CC-SPN and AF-SPN displayed almost identical fluorescence intensities at 810 nm. The PA signals of uSPN, CC-SPN and AF-SPN at 680 nm were determined at a series of concentrations, showing their PA signals were almost the same at the same concentration (Figure 2h). Also, the good linear relationship between the PA intensities and the concentrations was observed for all SPNs, indicating the feasibility for the signal quantification. The photothermal and photodynamic properties of these SPNs were then investigated. Since the NIR light could allow deeper tissue-penetration depth than the short-wavelength light due to its lower tissue absorption and scattering,[53] a NIR laser at 808 nm was used for both PTT and PDT. The temperatures of uSPN, CC-SPN and AF-SPN solutions at the same concentration gradually increased with irradiation time and reached the maximal photothermal temperature at ~51.0 ℃ at 360 s (Figure 2i). The temperature increase curves were almost the same for these nanoparticles. The photothermal conversion efficiencies of CC-SPN and AF-SPN were calculated to be 27.7 and 26.7%, respectively, similar to that of uSPN (26.3%). Such a similarity was due to the little influence of cell-membrane coatings on the heat absorption

and dissipation.[54-56] The photothermal conversion efficiencies of these SPNs were higher than that of other commonly used PTT agents including Au nanorods (17%),[49] CuS nanocrystals (25.7%),[57] and MoS_2 nanosheets (24.3%),[58] making them better phototherapeutic agents for cancer treatment. Additionally, all SPNs exhibited excellent photothermal stability as their maximal photothermal temperatures remained nearly the same after at least five heating and cooling circles (Figure S4, Supporting Information). Generation of $^1O_2$ for these SPNs under NIR laser irradiation at 808 nm was quantified using singlet oxygen sensor green (SOSG) as a $^1O_2$ indicator. With laser irradiation, the fluorescence intensity of SOSG gradually increased in a similar tendency for uSPN, CC-SPN and AF-SPN (Figure 2j). Using indocyanine green (ICG, $\Phi\Delta = 0.2\%$) as the reference,[59] the $^1O_2$ generation efficiency ($\Phi\Delta$) was estimated to be 3.53% for CC-SPN and 3.51% for AF-SPN, which were almost the same as that of uSPN (3.27%). These data clearly proved that the cell-membrane camouflages did not have obvious impact on the optical, photothermal and photodynamic properties of SPNs.

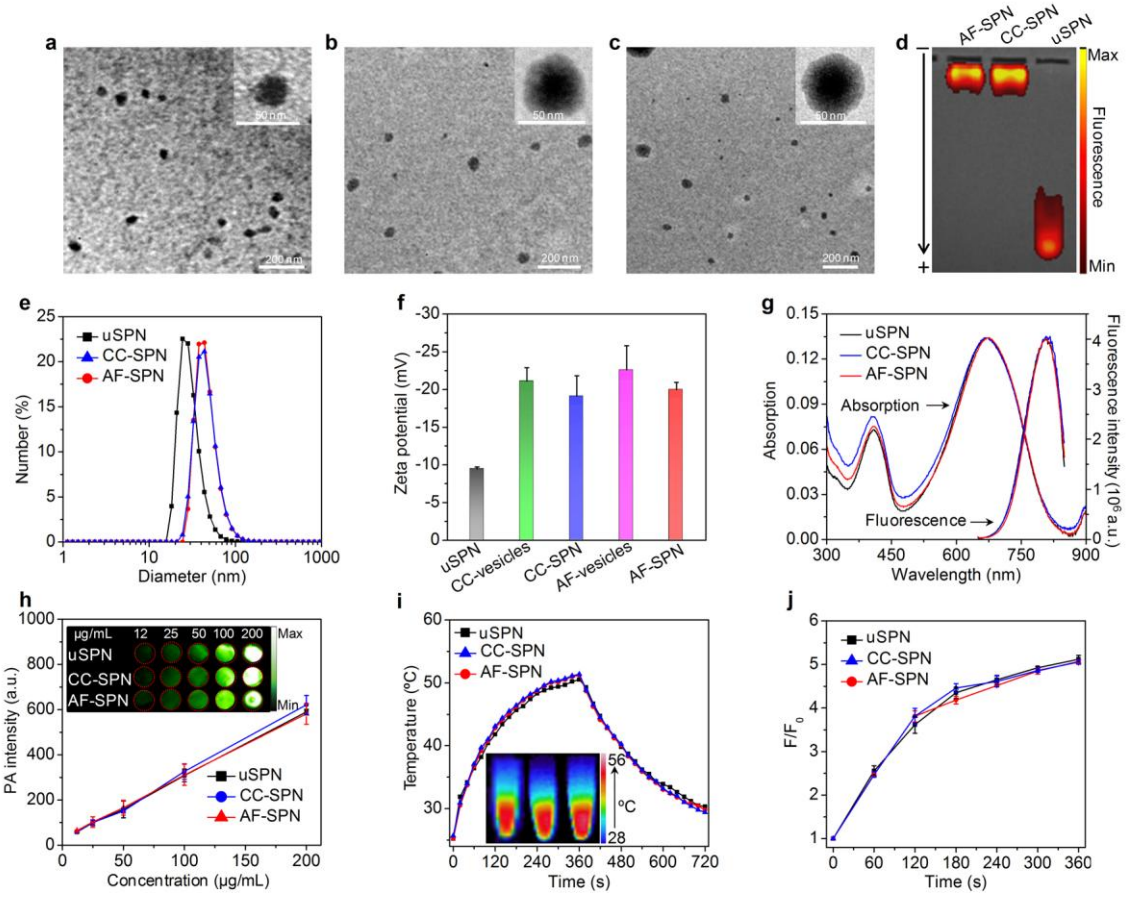

Figure 2. *In vitro* characterization of cell membrane coated SPNs. Representative TEM images of uSPN (a), CC-SPN (b) and AF-SPN (c). (d) Agarose gel electrophoresis of uSPN, CC-SPN and AF-SPN. SPNs in the gel were visualized using IVIS fluorescence imaging. (e) Dynamic light scattering (DLS) profiles of uSPN, CC-SPN and AF-SPN. (f) Zeta potentials of uSPN, CC-vesicles, CC-SPN, AF-vesicles and AF-SPN. (g) UV-vis absorption and fluorescence spectra of uSPN, CC-SPN and AF-SPN. (h) The PA intensities at 680 nm as a function of concentrations of uSPN, CC-SPN and AF-SPN. Inserts were the PA images of uSPN, CC-SPN and AF-SPN at different concentrations. (i) Photothermal temperatures of uSPN, CC-SPN and AF-SPN solutions as a function of laser irradiating time (power density = 1.0 W/cm^2, [SPN] = 15.0 μg/mL). Inserts were the thermal images of uSPN, CC-SPN and AF-SPN (from left to right) at their respective maximal temperatures. (j) The generation of $^1O_2$ determined by increased fluorescence intensity of SOSG for uSPN, CC-SPN and AF-SPN as a function of laser irradiating time (power density = 1.0 W/cm^2, [SPN] = 15.0 μg/mL).

After confirming the cell membrane coatings, the homologous targeting abilities of these SPN-based nanocamouflages toward AF cells and 4T1 cancer cells were studied. Similar with uSPN, CC-SPN and AF-SPN had negligible cytotoxicity against both AF cells and 4T1 cancer cells, even after incubation at a high concentration up to 50.0 μg/mL (Figure S5, Supporting Information). Confocal fluorescence imaging revealed that in the AF cell groups, the strongest nanoparticle fluorescence signal was observed for the AF-SPN treatment (Figure 3a); in contrast, the strongest nanoparticle fluorescence signal in the 4T1 cancer cell groups was detected for the CC-SPN treatment (Figure 3a). Flow cytometry was used to further quantify the cellular uptake of SPNs by different cell lines including AF cells, non-activated fibroblasts, 4T1 cancer cells, normal chondrocytes and other non-specific cancer cells (HeLa cells and SKOV3 cells). For the AF cell groups, AF-SPN-treated AF cells had the mean fluorescence intensity (MFI) that was 3.9- and 2.5-fold higher than that for uSPN- and CC-SPN-treated cells, respectively (Figure 3d,e). Although the MFI of AF-SPN treated non-activated fibroblasts was higher than that for uSPN- and CC-SPN treated cells (2.6- and 2-fold, respectively) (Figure S6a, Supporting Information), it was 1.7-fold lower than that of AF-SPN treated AF cells (Figure 3e). This confirmed our design, showing that AF-SPN had a favorable targeting towards AF cells over non-activated fibroblasts. Moreover, although CC-SPN had the highest MFI for the 4T1 cancer cell groups (Figure 3f,g), the MFI of AF-SPN-treated 4T1 cancer cells was 1.3-fold higher than that for uSPN-treated 4T1 cancer cells. By contrast, the MFI of normal chondrocytes, HeLa cancer cells and SKOV3 cancer cells after treatments with uSPN, CC-SPN and AF-SPN, respectively, did not have obvious difference (Figure S6b-d, Supporting Information). These data indicated that cell-membrane coatings endowed SPNs with the homologous targeting capability toward their source cells (Figure 3b,c), which was consistent with previous reports.[24, 60] In particular, surface coating of

AF cell membrane not only led to the specific targeting towards AF cells, but also facilitated the nanoparticle internalization into cancer cells. Because AF cells are referred as cancer-associated fibroblasts in tumor microenvironment,[61] AF-SPN should have the homogenous targeting capability to cancer-associated fibroblasts.

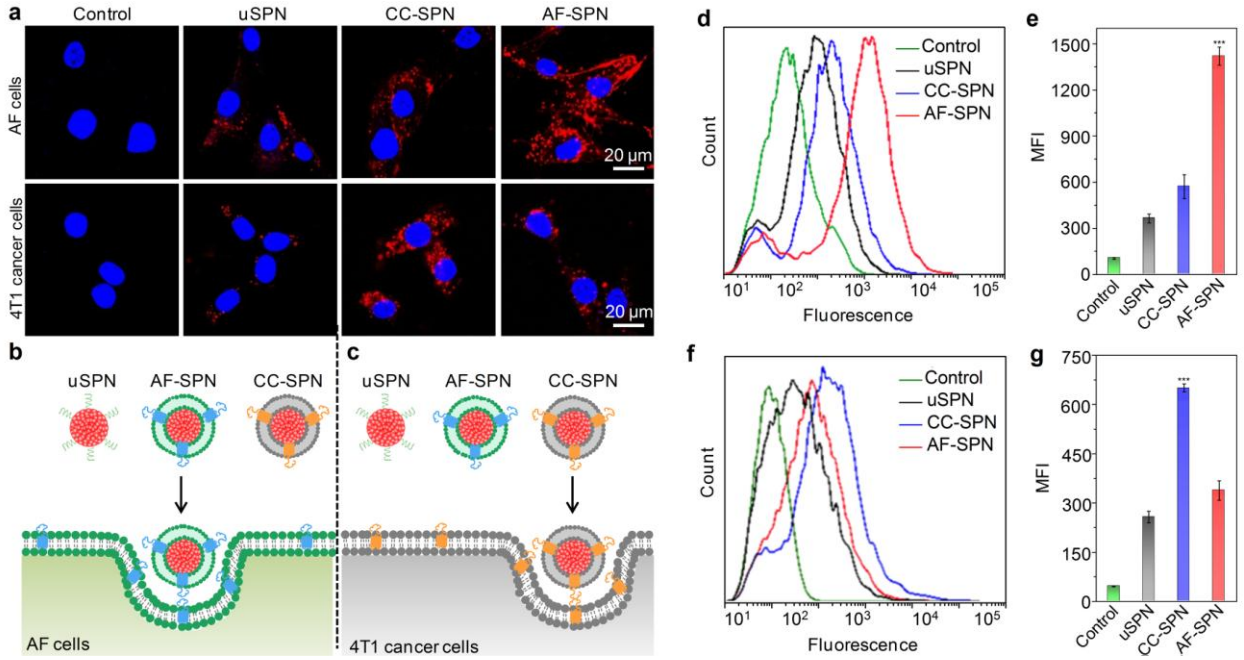

Figure 3. *In vitro* homologous targeting of cell membrane coated SPNs. (a) Confocal fluorescence images of AF cells and 4T1 cancer cells after incubation with uSPN, CC-SPN or AF-SPN ([SPN] = 15.0 μg/mL) for 12 h. The red fluorescence indicated nanoparticles and cell nucleus (blue) were stained by 4',6-diamidino-2-phenylindole (DAPI) (Scar bar = 20 μm). (b) Schematic illustration of homologous targeting of AF-SPN toward AF cells. (c) Schematic illustration of homologous targeting of CC-SPN toward 4T1 cancer cells. Flow cytometry analysis (d) and corresponding MFI (e) of AF cells after treatments with uSPN, CC-SPN or AF-SPN for 12 h ([SPN] = 15.0 μg/mL) (***$p < 0.001$, n = 3). Flow cytometry analysis (f) and corresponding MFI (g) of 4T1 cancer cells after treatments with uSPN, CC-SPN or AF-SPN for 12 h ([SPN] = 15.0 μg/mL) (***$p < 0.001$, n = 3).

To demonstrate the photodiagnostic potential of nanocamouflages for xenograft tumors in living mice, SPNs were systematically injected into 4T1 tumor-bearing nude mice through tail vein and their NIR fluorescence and PA images were obtained and quantified. Obvious fluorescence signals were observed in the tumor areas even at 2 h post-injection, and the fluorescence intensities gradually increased over time and reached the maximums at 48 h post-injection for all of these SPNs (Figure 4a,b). However, AF-SPN injected mice had much higher fluorescence signal in tumor areas as compared with uSPN and CC-SPN injected mice at each post-injection time point. In particular, at = 48 h post-injection, the tumor fluorescence intensity of AF-SPN injected mice was 1.5- and 1.3-fold higher than that of uSPN and CC-SPN injected mice, respectively. Note that uSPN, CC-SPN and AF-SPN had similar biodistribution in living mice regardless of their diameters and surface structures (Figure S7, Supporting Information). The PA signals of tumors gradually increased after injection of SPNs and the maximal PA intensity enhancement (ΔPA) in tumor regions were observed at 48 h (Figure 4c,d). At this time point, the ΔPA intensity of tumors for AF-SPN injected mice was 1.8- and 1.5-fold higher relative to that for uSPN and CC-SPN injected mice, respectively, consistent with the fluorescence imaging data. The enhanced NIR fluorescence and PA signals in tumor regions for AF-SPN injected mice should be attributed to the improved tumor accumulation of AF-SPN, because uSPN, CC-SPN and AF-SPN displayed the same fluorescence and PA intensities at the same concentration.

To visualize the nanoparticles in tumor, confocal fluorescence imaging of tumor slices was carried out at 48 h post-injection. The fluorescence signals of nanoparticles were clearly observed for SPN-injected mice. The tumor slices of AF-SPN injected mice had the highest fluorescence signal among these groups (Figure 4e and Figure S8, Supporting Information),

which was consistent with the *in vivo* NIR fluorescence and PA imaging data. These results reflected that the homologous targeting ability of AF-SPN toward cancer-associated fibroblasts occurred in living mice (Figure 4f), and subsequently facilitated its accumulation into tumors.[9, 24] Moreover, although CC-SPN had the ability to target cancer cells, it was limited by the barriers such as abundant cancer-associated fibroblasts in the tumor microenvironment, making its tumor accumulation marginally higher than non-targeting uSPN (Figures 4b,d).

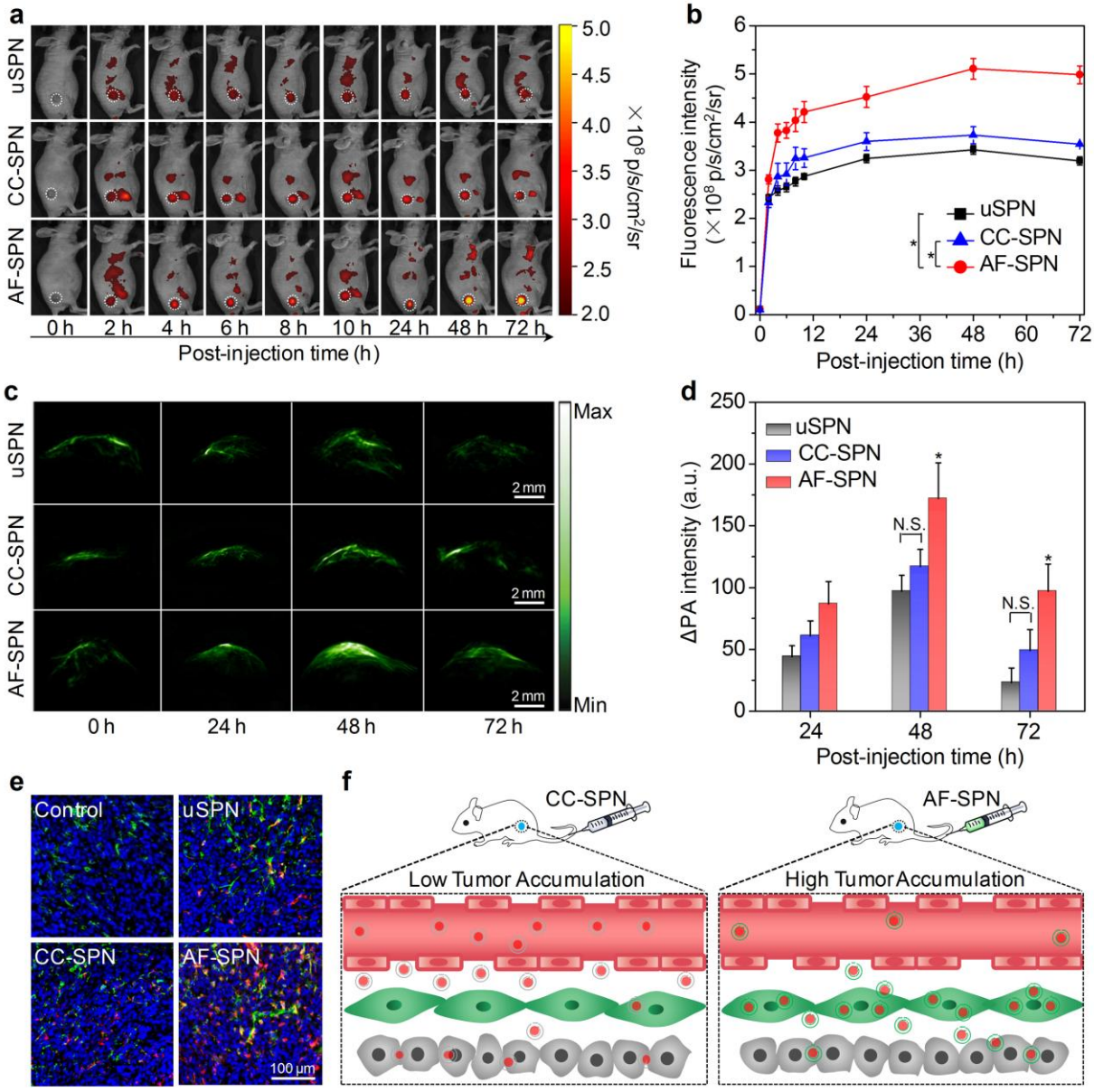

Figure 4. *In vivo* fluorescence and PA imaging of tumors in living mice. (a) *In vivo* NIR fluorescence images of 4T1 tumor-bearing mice at different time points after systemic administration of uSPN, CC-SPN and AF-SPN ([SPN] = 200.0 μg/mL, 0.2 mL) *via* the tail vein injection. The tumor was on the right side of the back as indicated by the white dashed circles. (b) Quantification of fluorescence intensities of tumor regions as a function of post-injection time after systemic administration of uSPN, CC-SPN and AF-SPN *via* the tail vein injection (*p < 0.05, n = 3). (c) Representative PA maximum imaging projection (MIP) images of 4T1 tumors in living mice at 0, 24, 48 and 72 h after systemic administration of uSPN, CC-SPN and AF-SPN ([SPN] = 200.0 μg/mL, 0.2 mL) *via* the tail vein injection. (d) Quantification of the enhanced PA intensities at 680 nm of tumors as a function of post-injection time of uSPN, CC-SPN and AF-SPN (N.S., no significance, *p < 0.05, n = 3). (e) Confocal fluorescence images of tumor slices from mice after systemic administration of saline (Control), uSPN, CC-SPN and AF-SPN ([SPN] = 200.0 μg/mL, 0.2 mL) at the post-injection time of 48 h. The red fluorescence indicated nanoparticles, cell nucleis (blue) were stained by DAPI, and blood vessels (green) were stained by Alexa Fluor 488 conjugated anti-CD31 antibody (scale bar = 100 μm). (f) Schematic illustration of the accumulation of CC-SPN and AF-SPN into tumors after systemic administration.

With its enhanced accumulation in tumor tissues, AF-SPN was used for *in vivo* phototherapy of xenografted 4T1 tumor models and compared with uSPN and CC-SPN. To reduce the side effects, the power density of NIR laser was used at its maximum permissible exposure (0.3 W/cm^2).[62] At 48 h post-injection, tumors were exposed to laser irradiation at 808 nm for 5 min and the temperature increases of tumor were monitored as a function of laser irradiation time (Figure 5a,b). At each time point, the mean tumor temperature of AF-SPN injected mice was much higher than that of saline, uSPN, and CC-SPN injected mice. In particular, the maximal tumor temperature after 5 min of laser irradiation was 50 ℃ for AF-SPN injected mice, which was 4.0, 6.0, and 14.0 ℃ higher than that for CC-SPN, uSPN, and saline injected mice, respectively. To confirm the PDT effect, immunofluorescence staining of protein sulfenic acids,

a biomarker for oxidized proteins,[63] was used to visualize the PDT induced damage. Obvious green fluorescence signals were observed in the tumors of SPN injected mice with laser irradiation (Figure 5c). Moreover, the green fluorescence signal for AF-SPN treated tumors was much stronger relative to uSPN and CC-SPN treated tumors. In contrast, nearly no green fluorescence signals could be detected in the saline injected mice with laser irradiation or the SPN injected mice without laser irradiation (Figure 5c and Figure S9, Supporting Information). Such increment in the heat and oxidative stress generation for AF-SPN injected mice relative to uSPN and CC-SPN injected mice should be attributed to the improved accumulation of AF-SPN in tumors through homologous targeting to cancer-associated fibroblasts in tumor microenvironment.

To evaluate the *in vivo* therapeutic efficiency of phototherapy, the volumes of tumors after treatments were recorded for 14 days (Figure 5d). The growth rates of tumors for SPN injected mice without NIR laser irradiation were similar to that of tumors for saline injected control mice. With laser irradiation, the tumor growth of mice after injection with uSPN, CC-SPN and AF-SPN was inhibited to different extent as compared to the control mice. Noted that AF-SPN exhibited the best efficiency of phototherapy as it completely ablated the tumors, while uSPN and CC-SPN failed to do so (Figure 5d,e). Moreover, all the SPN-mediated phototherapy did not induce any toxicity to living mice because no obvious changes in their body weights were observed (Figure S10, Supporting information).

To further verify the therapeutic effects, tumors after 2 days of treatments were extracted and sectioned for immunofluorescence caspase-3 staining and hematoxylin and eosin (H&E) staining. Confocal fluorescence images revealed that stronger green fluorescent signals could be observed in the tumor slides for AF-SPN injected mice relative to those for uSPN and CC-SPN injected

mice after NIR laser irradiation (Figure 5f), indicating higher level of apoptosis induced by AF-SPN mediated phototherapy. From H&E staining images, more necrotic cells were found in the tumor slides of AF-SPN injected mice as compared to uSPN and CC-SPN injected mice with NIR laser irradiation (Figure 5g), while other groups showed no obvious cell necrosis. These immunofluorescence and histological analysis suggested that AF-SPN outperformed uSPN and CC-SPN in cancer phototherapy. In addition, physiological morphology of major organs (heart, liver, spleen, lung, and kidney) and skin in the mice after phototherapy was assessed by H&E staining. The structures and morphologies of these organs and NIR laser irradiated skin in the treated mice were almost the same as those in the saline injected control mice, and no noticeable histopathological damage was observed (Figure S11, Supporting Information), implying the favorable compatibility of SPN-mediated phototherapy.

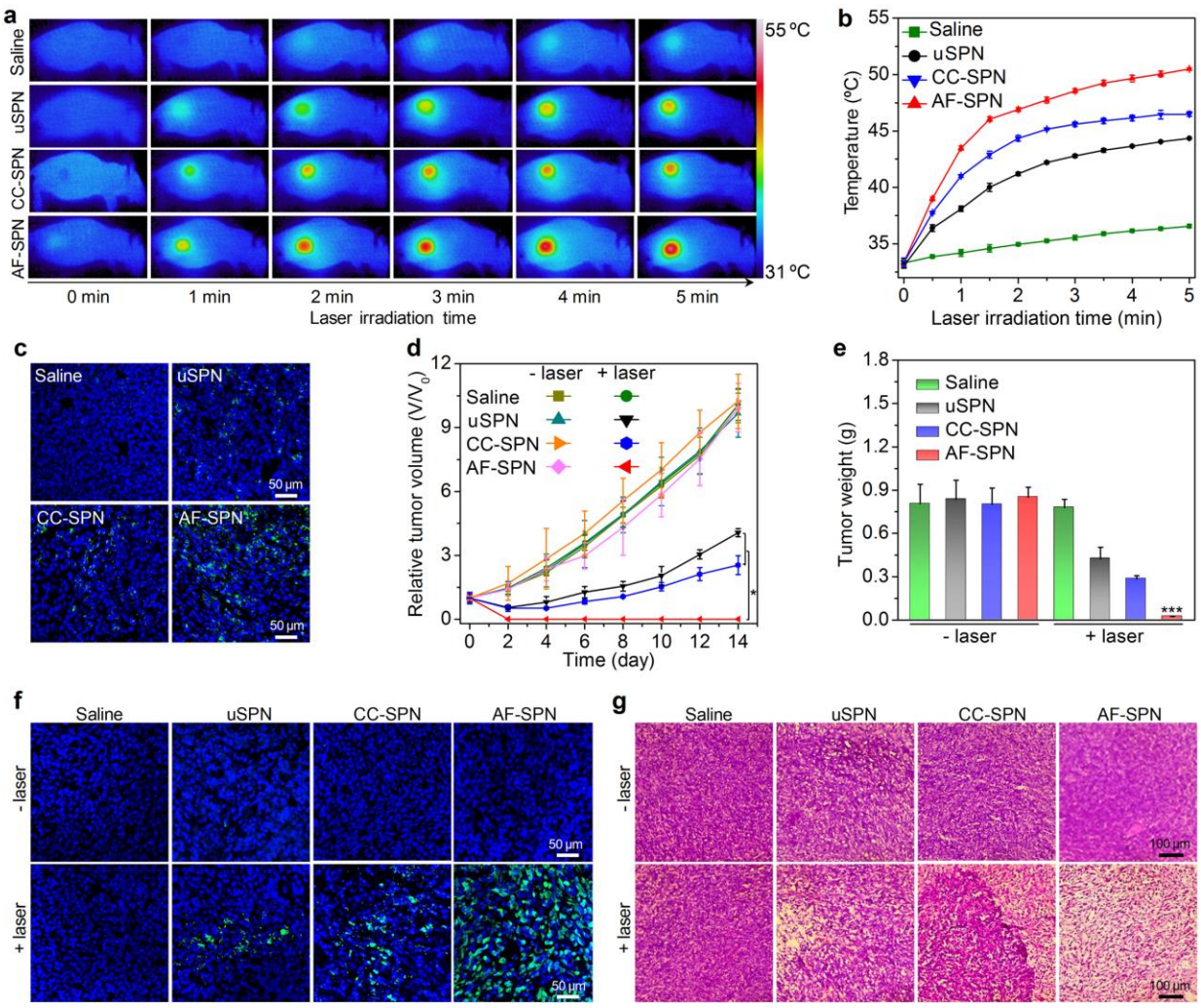

Figure 5. *In vivo* SPN-mediated phototherapy of tumors. (a) IR thermal images of 4T1 tumor-bearing mice under NIR laser irradiation at 808 nm with the laser power of 0.3 W/cm^2 for 5 min. The laser irradiation was performed at 48 h post-injection time after systemic administration of saline, uSPN, CC-SPN and AF-SPN ([SPN] = 200.0 μg/mL, 0.2 mL) *via* the tail vein injection. (b) Mean temperatures of tumors as a function of laser irradiation time after systemic administration of saline, uSPN, CC-SPN and AF-SPN. (c) Immunofluorescence staining with antisulfenic acid antibody of tumors in living mice after systemic administration of saline, uSPN, CC-SPN and AF-SPN after a NIR laser irradiation for 5 min. The green fluorescence indicated the signal from antisulfenic acid staining and the blue fluorescence was from DAPI stained cell nucleus (scale bars = 50 μm). Tumor growth curves (d) and mean tumor weights (e) in living mice after systemic administration of saline, uSPN, CC-SPN and AF-SPN with or without NIR

laser irradiation for 5 min (*p < 0.05, ***p < 0.001, n = 3). (f) Immunofluorescence caspase-3 staining images of tumors in living mice after uSPN-, CC-SPN-, and AF-SPN-mediated phototherapy. The green fluorescence indicated the signal from caspase-3 staining, and blue fluorescence was from DAPI stained cell nucleus (scale bars = 50 μm). (g) Histological H&E staining of tumors in living mice after systemic administration of saline, uSPN, CC-SPN and AF-SPN with or without NIR laser irradiation for 5 min (scale bars = 100 μm).

CONCLUSIONS

In summary, we developed a biomimetic SPN-based nanocamouflage (AF-SPN) that could specifically target to cancer-associate fibroblasts in tumor microenvironment for enhanced multimodal cancer phototheranostics. AF-SPN was prepared through co-extrusion of SPNs and AF-derived cell membranes, and the cell membrane camouflage did not compromise their NIR fluorescence, PA, photothermal and photodynamic properties. Through the homologous targeting binding mechanism, AF-SPN preferentially targeted cancer-associate fibroblasts, resulting in higher accumulation in tumor tissues than both the uncoated (uSPN) and cancer cell membrane coated counterparts (CC-SPN). As such, AF-SPN acted as the optimal phototheranostic nanoagents to provide amplified NIR fluorescence and PA signals for tumor imaging, and enhanced phototherapeutic efficiency for cancer treatment. This study presents an example of a cell membrane coated biomimetic organic phototheranostic nanoagent that targets the component in tumor microenvironment, which contributes to the design of therapeutic strategies to overcome the delivery barriers in tumors. In addition, other pharmaceutical and imaging agents can be loaded into such biomimetic nanocamouflages, bringing in multimodal theranostic platforms beyond optical imaging and phototherapy.

EXPEIMENTAL SECTION

Chemicals. PCPDTBT was purchased from Luminescence Technology Corp. (Hsin Chu, Taiwan). Singlet oxygen sensor green (SOSG) was provided by Molecular Probes Lnc. (Carlsbad, CA, USA). Agarose powder (Certified Molecular Biology Agarose) was purchased from Bio-Rad, Hercules, CA, USA). Alexa Fluor® 488 conjugated goat anti-rabbit IgG, anti-CD31 antibody and anti-caspase-3 antibody were purchased from Abcam Inc. (Cambridge, CA, USA). 3-(4,5-Dimethylthiazol-2-yl)-5-(3-carboxymethoxyphenyl)-2-(4-sulfophenyl)-2H-tetrazolium, inner salt (MTS) solution was obtained from Promega Corp. (Madison, WI, USA). All the other chemicals were purchased from Sigma-Aldrich (St. Louis, MO, USA).

Characterization Techniques. TEM images were captured by a JEOL 1400 transmission electron microscope (Tokyo, Japan). Fluorescence spectra were recorded by a Fluorolog 3-TCSPC spectrofluorometer (Horiba Jobin Yvon). Diameter and zeta potential were measured on a Malvern Nano-ZS Particle Sizer (Malvern Instruments, Southborough, UK). UV-Vis spectra were recorded using an UV-2450 spectrophotometer (Shimadzu, Japan). *In vitro* PA signal measurement was performed on an optical parametric oscillator (Continuum, Surelite). *In vivo* fluorescence imaging was carried out on an IVIS imaging system (IVIS-CT machine, PerkinElmer).

Preparation of uSPN. PCPDTBT (0.25 mg) and PEG-b-PPG-b-PEG (50.0 mg) were co-dissolved in 1.0 mL tetrahydrofuran (THF) and the resultant solution was dropped into 10.0 mL mixture solution of THF and water (v/v = 1:9) under sonication for 2 min. After the formation of uSPN, THF was removed by a nitrogen flow and the remaining products were filtrated through 0.22 μm PVDF filter. Ultrafiltration (3500 rpm, 25 min) was carried out to concentrate the obtained uSPN and the concentration was then determined using an UV-Vis spectrophotometer.

Preparation of AF-SPN. Normal fibroblasts were cultured in DMEM cell culture medium supplemented with 10% FBS at 37 ℃ and 5% CO_2. After 80% of confluence, normal fibroblasts were treated with TGF-β1 (100.0 ng/mL) in DMEM medium supplemented with 1% FBS for 2 days to induce them into AF cells.[51] Afterward, AF cells were collected and washed three times with PBS. To obtain AF-derived vesicles, the collected cells were dispersed in membrane protein extraction buffer solution, treated with sonication for 1 min, and then extruded 15 times through 400 nm polycarbonate porous membranes using an Avanti mini extruder (Avanti Polar Lipids, USA). To coat cell membranes onto the surface of uSPN, AF-derived vesicles (1.0 mL) were mixed with uSPN solution (1.0 mL), and the mixture was extruded 15 times through 100 nm polycarbonate porous membranes using an Avanti mini extruder. The excess vesicles were removed by centrifugation and the obtained AF-SPN was stored at 4 ℃ for further use. 4T1 cancer cell membrane coated SPN (CC-SPN) was prepared in a similar manner and used as a control for the further experiments.

Agarose Gel Electrophoresis. Agarose powder was dissolved in 1× Tris/boric acid/ethylenediaminetetraacetic acid (EDTA) (TBE) buffer and used to prepare agarose gels (2%). The gels were immersed in 1× TBE buffer. The solutions of SPNs (60.0 μg/mL, 40.0 μL) were mixed with 10.0% SDS solution (4.0 μL) and 10× loading buffer (5.0 μL). Then SPN solutions were loaded in each well of the gels and electrophoresed on a horizontal electrophoresis system at 120 V for 40 min. The obtained gels were visualized using an IVIS living imaging system.

SDS-PAGE. CC-derived vesicles, CC-SPN, AF-derived vesicles, AF-SPN and uSPN with the loading buffer were heated at 98 ℃ for 10 min and mixed with SDS buffer, respectively. Afterwards, 25.0 μL of sample was loaded into each well of 10.0% SDS-polyacrylamide gels and

run at 90 V for 2 h. The obtained gels were subsequently stained with Commassie Blue for 6 h and then washed overnight to visualize protein bands.

***In Vitro* Photothermal Property.** 200.0 μL PBS solutions of uSPN, CC-SPN and AF-SPN at the concentration of 15.0 μg/mL were put into microtubes and irradiated using an 808 nm laser (CNI Optoelectronics Tech. Ltd., China) for 6 min (power density = 1.0 W/cm^2). Then the laser was turned off and samples were naturally cooled for another 6 min. An IR thermal camera (FLIR T420) was used to monitor the temperature changes every 20 s. Five cycles of laser on/off were carried out to study photothermal stability of SPNs. Photothermal conversion efficiencies of SPNs were calculated according to our previously reported method.[49]

***In Vitro* $^1O_2$ Generation Measurement.** The generation of $^1O_2$ under 808 laser irradiation was confirmed using a commercial chemical reagent, SOSG.[64] 1.0 mL of uSPN, CC-SPN and AF-SPN solution (15.0 μg/mL) containing 0.5 μM of SOSG was irradiated by an 808 nm laser for different time (1-6 min). At each time interval, fluorescence intensities at 520 nm (F) of samples were measured on a Fluorolog 3-TCSPC spectrofluorometer. Samples without laser irradiation were used as the controls and their fluorescence intensities at 520 nm (F_0) were recorded. The generation of $^1O_2$ was expressed as fluorescence enhancement (F/F_0). Photosensitizer ICG was used as the reference to quantify the $^1O_2$ generation efficiency by the following equation: $\Phi\Delta_{SPN} = (r_{SPN}/Abs_{SPN})/(r_{ICG}/Abs_{ICG})*\Phi\Delta_{ICG}$. Where r_{SPN} and r_{ICG} are the SOSG reaction rate with $^1O_2$ generated from SPNs and ICG, which can be directly obtained from time-dependent fluorescence enhancement of SOSG, respectively; Abs_{SPN} and Abs_{ICG} are the corresponding absorbance of SPNs (15.0 μg/mL) and ICG (15.0 μg/mL) at 808 nm, respectively; $\Phi\Delta_{ICG}$ is the known $^1O_2$ generation efficiency of ICG, which is 0.2%.

***In Vitro* Cytotoxicity Assay.** AF cells and 4T1 cancer cells cultured in 96-well plates were incubated with uSPN, CC-SPN or AF-SPN at different concentrations for 24 h. Then the cells were cultured in DMEM medium containing 20.0% MTS for another 4 h. To calculate the cell viability, the absorbance of cell culture medium at 490 nm was measured using a SpectraMax M5 microplate reader.

***In Vitro* Cellular Uptake Assay.** AF cells and 4T1 cancer cells cultured in confocal cell culture dishes (4×10^4 cells/dish) were incubated in DMEM cell culture medium containing uSPN, CC-SPN and AF-SPN at the concentration of 15.0 μg/mL for 12 h, respectively. The treated cells were washed, fixed and then stained with DAPI. Then a LSM800 confocal laser scanning microscope (Carl Zeiss, Germany) was used to capture the fluorescence images.

Flow cytometry was performed to quantify the cellular uptake. AF cells, normal fibroblasts, normal chondrocytes, 4T1 cancer cells, HeLa cancer cells and SKOV3 cancer cells were incubated with uSPN, CC-SPN and AF-SPN ([SPN] = 15.0 μg/mL) for 12 h, respectively. Then the treated cells were successively washed, trypsinized, collected, resuspended in PBS and used for cellular uptake analysis on a FACSCalibur flow cytometer (Becton Dickinson, USA).

Animals and Tumor Models. All animal experiments were conducted in accordance with the guidelines established by the Institutional Animal Care and Use Committee (IACUC), Sing Health. 0.1 mL DMEM containing 2×10^6 4T1 cells were subcutaneously implanted into right side of the back of 4- to 6-week-old female NCr nude mice to establish the xenografted tumor models. 4T1 tumor-bearing mice were used for fluorescence and PA imaging and cancer therapy experiments after 7 days of growth.

***In Vivo* NIR Fluorescence Imaging.** For fluorescence imaging, 4T1 tumor-bearing mice were anesthetized using 2% isoflurane in oxygen and then injected with uSPN, CC-SPN or AF-SPN

([SPN] = 200.0 μg/mL, 0.2 mL) *via* the tail vein, respectively (n = 3). Fluorescence whole-animal imaging was carried out on an IVIS imaging system. Before (0 h) and after administration of SPNs at designated time points, fluorescence whole-animal images of mice were collected. A Living Image software was used to quantify the fluorescence intensities of tumors in different mice.

***Ex Vivo* Biodistribution.** At 72 h post-injection time point, 4T1 tumor-bearing mice in each group were euthanized. Kidney, lung, spleen, liver, heart and tumor were extracted and used for *ex vivo* fluorescence imaging by an IVIS imaging system. The fluorescence intensities of these organs and tumors were quantified to study the biodistribution of nanoparticles.

***In Vivo* PA imaging.** The 4T1 tumor-bearing mice were anesthetized with 2% isoflurane in oxygen. After that, uSPN, CC-SPN or AF-SPN (0.2 mL, [SPN] = 200.0 μg/mL) was injected into the mice *via* the tail vein, respectively (n = 3). PA images of tumor regions in the injected mice was acquired before (0 h) and after injection of SPNs at designated time points using a multispectral optoacoustic tomography scanner (MSOT, iThera medical, Germany) at 680 nm.

***In Vivo* Cancer Therapy.** 4T1 tumor-bearing mice were intravenously injected with 0.2 mL of saline, uSPN, CC-SPN or AF-SPN ([SPN] = 200.0 μg/mL) (n = 3). At 48 h post-injection time point, the tumors of mice were irradiated using an 808 nm laser for 5 min (0.3 W/cm^2) and an IR thermal camera was used to record the tumor temperature changes every 30 s. To monitor the therapeutic efficiency and biosafety, tumor sizes and body weights of mice were measured every other day for 14 days. The tumor volume was calculated as follows: $V = (\text{length}) \times (\text{width})^2/2$. Relative tumor volume was calculated as V/V_0 (V_0 was the initial tumor volume).

Immunofluorescence Staining of Protein Sulfenic Acids. 4T1 tumor-bearing mice were intravenously injected with 0.2 mL of saline, uSPN, CC-SPN or AF-SPN ([SPN] = 200.0

μg/mL). After 48 h, the tumors were exposed under an 808 nm laser irradiation for 5 min (0.3 W/cm^2). Mice were subsequently euthanized and the collected tumors were fixed in 4% formalin, dehydrated with 30% sucrose solution and then cut into 10-μm sections using a cryostat (Leica, CM1950). The slides of tumor samples were stained with anticysteine sulfenic acid antibody (no. 07-2139, Merck, 1:3000) according to our previously reported protocol.[63]

Histological Analysis. After 48 h of cancer therapy, the mice in each group were euthanized to extract tumors. The collected tumor tissues were fixed at 4 ℃ for 48 h and dehydrated with sucrose solution (30%) for 24 h. The dehydrated tumor tissues were embedded in frozen optimal cutting temperature (O.C.T.) medium and cut into 10-μm sections using a cryostat (Leica, CM1950). For immunofluorescence caspase-3 staining, the sections were dried overnight and washed with PBS containing 0.1% Triton X-100. The sections were treated with bovine serum albumin (BSA) solution (3%) at 25 ℃ for 1 h and washed again with PBS. The sections were then incubated with anti-caspase-3 antibody solution at 4 ℃ overnight. Unbound antibody was removed by PBS washing and the sections were then treated with Alexa Fluor 488 conjugated goat anti-rabbit IgG at 25 ℃ for 1 h. The sections were washed with PBS again and then stained with DAPI at 25 ℃ for 20 min. The stained sections were observed under a LSM800 confocal laser scanning microscope. As for H&E staining, the fixed tumors and tissues were dehydrated in a series of ethanol solution, embedded in paraffin and then cut into sections with a thickness of 10 μm. The sections were washed with ethanol, and immersed in hematoxylin working solution for 3 min and then in eosin working solution for 1 min. The stained slices were washed with water and observed by a Nikon ECLIPSE 80i microscope (Nikon Corporation, Towa Optics, New Delhi, India).

Statistical Analysis. All experiments were repeated in triplicate (n = 3) and the results were expressed as mean ± standard deviations (SD). Statistical comparisons between two groups were determined using One-way ANOVA statistical analysis. A p value of 0.05 was selected as the level of significance, and the data were classified according to their p values and denoted by (*) for $p < 0.05$, (**) for $p < 0.01$, and (***) for $p < 0.001$.

ASSOCIATED CONTENT

Supporting Information.

The Supporting Information is available free of charge on the ACS Publications website at DOI: 10.1021/acsnano.XXXXX.

Characterization of nanoparticles including fluorescence spectra, SDS-PAGE, colloidal stability, photothermal stability, cell viability, flow cytometry assay, *ex vivo* biodistribution, nanoparticle tumor accumulation, protein sulfenic acids immunofluorescence staining, body weights and H&E staining of major organs in treated mice can be found in the Supporting Information Available online (Figure S1−S11).

AUTHOR INFORMATION

Corresponding Author

*Email: kypu@ntu.edu.sg.

ACKNOWLEDGMENTS

K.P. thanks Nanyang Technological University (Start-Up grant: NTU-SUG: M4081627.120) and Singapore Ministry of Education (Academic Research Fund Tier 1: RG133/15 M4011559 and Academic Research Fund Tier 2 MOE20s16-T2-1-098) for the financial support. All the animal

experiments were conducted in compliance with the guidelines established by the Institutional Animal Care and Use Committee (IACUC), Sing Health.

REFERENCES

(1) Yu, J.; Yang, C.; Li, J.; Ding, Y.; Zhang, L.; Yousaf, M. Z.; Lin, J.; Pang, R.; Wei, L.; Xu, L.; Sheng, F.; Li, C.; Li, G.; Zhao, L.; Hou, Y. Multifunctional Fe_5C_2 Nanoparticles: A Targeted Theranostic Platform for Magnetic Resonance Imaging and Photoacoustic Tomography-Guided Photothermal Therapy. *Adv. Mater.* **2014**, *26*, 4114-4120.

(2) Liu, J.; Bu, W.; Shi, J. Chemical Design and Synthesis of Functionalized Probes for Imaging and Treating Tumor Hypoxia. *Chem. Rev.* **2017**, *117*, 6160-6224.

(3) Yang, K.; Feng, L.; Shi, X.; Liu, Z. Nano-Graphene in Biomedicine: Theranostic Applications. *Chem. Soc. Rev.* **2013**, *42*, 530-547.

(4) Cui, L.; Lin, Q.; Jin, C. S.; Jiang, W.; Huang, H.; Ding, L.; Muhanna, N.; Irish, J. C.; Wang, F.; Chen, J.; Zheng, G. A PEGylation-Free Biomimetic Porphyrin Nanoplatform for Personalized Cancer Theranostics. *ACS Nano* **2015**, *9*, 4484-4495.

(5) Zhang, L.; Gao, S.; Zhang, F.; Yang, K.; Ma, Q.; Zhu, L. Activatable Hyaluronic Acid Nanoparticle as a Theranostic Agent for Optical/Photoacoustic Image-Guided Photothermal Therapy. *ACS Nano* **2014**, *8*, 12250-12258.

(6) Zhao, X.; Yang, C.-X.; Chen, L.-G.; Yan, X.-P. Dual-Stimuli Responsive and Reversibly Activatable Theranostic Nanoprobe for Precision Tumor-Targeting and Fluorescence-Guided Photothermal Therapy. *Nat. Commun.* **2017**, *8*, 14998.

(7) Karimi, M.; Sahandi Zangabad, P.; Baghaee-Ravari, S.; Ghazadeh, M.; Mirshekari, H.; Hamblin, M. R. Smart Nanostructures for Cargo Delivery: Uncaging and Activating by Light. *J. Am. Chem. Soc.* **2017**, *139*, 4584-4610.

(8) Wang, S.; Zhao, J.; Yang, H.; Wu, C.; Hu, F.; Chang, H.; Li, G.; Ma, D.; Zou, D.; Huang, M. Bottom-Up Synthesis of WS_2 Nanosheets with Synchronous Surface Modification for Imaging Guided Tumor Regression. *Acta Biomater.* **2017**, *58*, 442-454.

(9) Chen, Z.; Zhao, P.; Luo, Z.; Zheng, M.; Tian, H.; Gong, P.; Gao, G.; Pan, H.; Liu, L.; Ma, A.; Cui, H.; Ma, Y.; Cai, L. Cancer Cell Membrane-Biomimetic Nanoparticles for Homologous-Targeting Dual-Modal Imaging and Photothermal Therapy. *ACS Nano* **2016**, *10*, 10049-10057.

(10) Zhu, M.; Sheng, Z.; Jia, Y.; Hu, D.; Liu, X.; Xia, X.; Liu, C.; Wang, P.; Wang, X.; Zheng, H. Indocyanine Green-Holo-Transferrin Nanoassemblies for Tumor-Targeted Dual-Modal Imaging and Photothermal Therapy of Glioma. *ACS Appl. Mater. Interfaces* **2017**, *9*, 39249-39258.

(11) Li, M.; Gao, Y.; Yuan, Y.; Wu, Y.; Song, Z.; Tang, B. Z.; Liu, B.; Zheng, Q. C. One-Step Formulation of Targeted Aggregation-Induced Emission Dots for Image-Guided Photodynamic Therapy of Cholangiocarcinoma. *ACS Nano* **2017**, *11*, 3922-3932.

(12) Fang, R. H.; Kroll, A. V.; Gao, W.; Zhang, L. Cell Membrane Coating Nanotechnology. *Adv. Mater.* **2018**, *30*, 1706759.

(13) Hu, Q.; Sun, W.; Qian, C.; Wang, C.; Bomba, H. N.; Gu, Z. Anticancer Platelet-Mimicking Nanovehicles. *Adv. Mater.* **2015**, *27*, 7043-7050.

(14) Yu, B.; Goel, S.; Ni, D.; Ellison, P. A.; Siamof, C. M.; Jiang, D.; Cheng, L.; Kang, L.; Yu, F.; Liu, Z.; Todd, E. B.; He, Q.; Zhang, H.; Cai, W. Reassembly of ^{89}Zr-Labeled Cancer Cell Membranes into Multicompartment Membrane-Derived Liposomes for PET-Trackable Tumor-Targeted Theranostics. *Adv. Mater.* **2018**, *30*, 1704934.

(15) Hu, Q.; Qian, C.; Sun, W.; Wang, J.; Chen, Z.; Bomba, H. N.; Xin, H.; Shen, Q.; Gu, Z. Engineered Nanoplatelets for Enhanced Treatment of Multiple Myeloma and Thrombus. *Adv. Mater.* **2016**, *28*, 9573-9580.

(16) Yang, R.; Xu, J.; Xu, L.; Sun, X.; Chen, Q.; Zhao, Y.; Peng, R.; Liu, Z. Cancer Cell Membrane-Coated Adjuvant Nanoparticles with Mannose Modification for Effective Anticancer Vaccination. *ACS Nano* **2018**, *12*, 5121-5129.

(17) Gao, M.; Liang, C.; Song, X.; Chen, Q.; Jin, Q.; Wang, C.; Liu, Z. Erythrocyte-Membrane-Enveloped Perfluorocarbon as Nanoscale Artificial Red Blood Cells to Relieve Tumor Hypoxia and Enhance Cancer Radiotherapy. *Adv. Mater.* **2017**, *29*, 1701429.

(18) Chen, W.; Zeng, K.; Liu, H.; Ouyang, J.; Wang, L.; Liu, Y.; Wang, H.; Deng, L.; Liu, Y. N. Cell Membrane Camouflaged Hollow Prussian Blue Nanoparticles for Synergistic Photothermal-/Chemotherapy of Cancer. *Adv. Funct. Mater.* **2017**, *27*, 1605795.

(19) Su, J.; Sun, H.; Meng, Q.; Yin, Q.; Tang, S.; Zhang, P.; Chen, Y.; Zhang, Z.; Yu, H.; Li, Y. Long Circulation Red-Blood-Cell-Mimetic Nanoparticles with Peptide-Enhanced Tumor Penetration for Simultaneously Inhibiting Growth and Lung Metastasis of Breast Cancer. *Adv. Funct. Mater.* **2016**, *26*, 1243-1252.

(20) Fu, Q.; Lv, P.; Chen, Z.; Ni, D.; Zhang, L.; Yue, H.; Yue, Z.; Wei, W.; Ma, G. Programmed Co-Delivery of Paclitaxel and Doxorubicin Boosted by Camouflaging with Erythrocyte Membrane. *Nanoscale* **2015**, *7*, 4020-4030.

(21) Su, J.; Sun, H.; Meng, Q.; Zhang, P.; Yin, Q.; Li, Y. Enhanced Blood Suspensibility and Laser-Activated Tumor-Specific Drug Release of Theranostic Mesoporous Silica Nanoparticles by Functionalizing with Erythrocyte Membranes. *Theranostics* **2017**, *7*, 523-537.

(22) Sun, H.; Su, J.; Meng, Q.; Yin, Q.; Chen, L.; Gu, W.; Zhang, P.; Zhang, Z.; Yu, H.; Wang, S.; Li, Y. Cancer-Cell-Biomimetic Nanoparticles for Targeted Therapy of Homotypic Tumors. *Adv. Mater.* **2016**, *28*, 9581-9588.

(23) Li, S.-Y.; Xie, B.-R.; Cheng, H.; Li, C.-X.; Zhang, M.-K.; Qiu, W.-X.; Liu, W.-L.; Wang, X.-S.; Zhang, X.-Z. A Biomimetic Theranostic O_2-Meter for Cancer Targeted Photodynamic Therapy and Phosphorescence Imaging. *Biomaterials* **2018**, *151*, 1-12.

(24) Zhu, J.; Zheng, D.; Zhang, M.; Yu, W.; Qiu, W.; Hu, J.; Feng, J.; Zhang, X. Preferential Cancer Cell Self-Recognition and Tumor Self-Targeting by Coating Nanoparticles with Homotypic Cancer Cell Membranes. *Nano Lett.* **2016**, *16*, 5895-5901.

(25) Rao, L.; Bu, L. L.; Meng, Q. F.; Cai, B.; Deng, W. W.; Li, A.; Li, K.; Guo, S. S.; Zhang, W. F.; Liu, W. Antitumor Platelet-Mimicking Magnetic Nanoparticles. *Adv. Funct. Mater.* **2017**, *27*, 1604774.

(26) Gao, C.; Lin, Z.; Wu, Z.; Lin, X.; He, Q. Stem-Cell-Membrane Camouflaging on Near-Infrared Photoactivated Upconversion Nanoarchitectures for *In Vivo* Remote-Controlled Photodynamic Therapy. *ACS Appl. Mater. Interfaces* **2016**, *8*, 34252-34260.

(27) Shen, S.; Li, H.-J.; Chen, K.-G.; Wang, Y.-C.; Yang, X.-Z.; Lian, Z.-X.; Du, J.-Z.; Wang, J. Spatial Targeting of Tumor-Associated Macrophages and Tumor Cells with a pH-Sensitive Cluster Nanocarrier for Cancer Chemoimmunotherapy. *Nano Lett.* **2017**, *17*, 3822-3829.

(28) Parodi, A.; Haddix, S. G.; Taghipour, N.; Scaria, S.; Taraballi, F.; Cevenini, A.; Yazdi, I. K.; Corbo, C.; Palomba, R.; Khaled, S. Z.; Martinez, J. O.; Brown, B. S.; Isenhart, L.; Tasciotti, E. Bromelain Surface Modification Increases the Diffusion of Silica Nanoparticles in the Tumor Extracellular Matrix. *ACS Nano* **2014**, *8*, 9874-9883.

(29) Stapleton, S.; Jaffray, D.; Milosevic, M. Radiation Effects on the Tumor Microenvironment: Implications for Nanomedicine Delivery. *Adv. Drug Delivery Rev.* **2017**, *109*, 119-130.

(30) Gong, H.; Chao, Y.; Xiang, J.; Han, X.; Song, G.; Feng, L.; Liu, J.; Yang, G.; Chen, Q.; Liu, Z. Hyaluronidase to Enhance Nanoparticle-Based Photodynamic Tumor Therapy. *Nano Lett.* **2016**, *16*, 2512-2521.

(31) Hu, Q.; Sun, W.; Lu, Y.; Bomba, H. N.; Ye, Y.; Jiang, T.; Isaacson, A. J.; Gu, Z. Tumor Microenvironment-Mediated Construction and Deconstruction of Extracellular Drug-Delivery Depots. *Nano Lett.* **2016**, *16*, 1118-1126.

(32) Chen, B.; Dai, W.; Mei, D.; Liu, T.; Li, S.; He, B.; He, B.; Yuan, L.; Zhang, H.; Wang, X.; Zhang, Q. Comprehensively Priming the Tumor Microenvironment by Cancer-Associated Fibroblast-Targeted Liposomes for Combined Therapy with Cancer Cell-Targeted Chemotherapeutic Drug Delivery System. *J. Controlled Release* **2016**, *241*, 68-80.

(33) Ji, T.; Ding, Y.; Zhao, Y.; Wang, J.; Qin, H.; Liu, X.; Lang, J.; Zhao, R.; Zhang, Y.; Shi, J.; Tao, N.; Qin, Z.; Nie, G. Peptide Assembly Integration of Fibroblast-Targeting and Cell-Penetration Features for Enhanced Antitumor Drug Delivery. *Adv. Mater.* **2015**, *27*, 1865-1873.

(34) Zhu, C.; Liu, L.; Yang, Q.; Lv, F.; Wang, S. Water-Soluble Conjugated Polymers for Imaging, Diagnosis, and Therapy. *Chem. Rev.* **2012**, *112*, 4687-4735.

(35) Wu, C.; Chiu, D. T. Highly Fluorescent Semiconducting Polymer Dots for Biology and Medicine. *Angew. Chem., Int. Ed.* **2013**, *52*, 3086-3109.

(36) Li, J.; Rao, J.; Pu, K. Recent Progress on Semiconducting Polymer Nanoparticles for Molecular Imaging and Cancer Phototherapy. *Biomaterials* **2018**, *155*, 217-235.

(37) Jiang, Y.; Pu, K. Advanced Photoacoustic Imaging Applications of Near-Infrared Absorbing Organic Nanoparticles. *Small* **2017**, *13*, 1700710.

(38) Lyu, Y.; Cui, D.; Sun, H.; Miao, Y.; Duan, H.; Pu, K. Dendronized Semiconducting Polymer as Photothermal Nanocarrier for Remote Activation of Gene Expression. *Angew. Chem., Int. Ed.* **2017**, *56*, 9155-9159.

(39) Zhu, H.; Fang, Y.; Zhen, X.; Wei, N.; Gao, Y.; Luo, K. Q.; Xu, C.; Duan, H.; Ding, D.; Chen, P.; Pu, K. Multilayered Semiconducting Polymer Nanoparticles with Enhanced NIR Fluorescence for Molecular Imaging in Cells, Zebrafish and Mice. *Chem. Sci.* **2016**, *7*, 5118-5125.

(40) Zhen, X.; Zhang, C.; Xie, C.; Miao, Q.; Lim, K. L.; Pu, K. Intraparticle Energy Level Alignment of Semiconducting Polymer Nanoparticles to Amplify Chemiluminescence for Ultrasensitive *In Vivo* Imaging of Reactive Oxygen Species. *ACS Nano* **2016**, *10*, 6400-6409.

(41) Xie, C.; Zhen, X.; Lyu, Y.; Pu, K. Nanoparticle Regrowth Enhances Photoacoustic Signals of Semiconducting Macromolecular Probe for *In Vivo* Imaging. *Adv. Mater.* **2017**, *29*, 1703693.

(42) Smith, B. R.; Gambhir, S. S. Nanomaterials for *In Vivo* Imaging. *Chem. Rev* **2017**, *117*, 901-986.

(43) Jiang, Y.; Upputuri, P. K.; Xie, C.; Lyu, Y.; Zhang, L.; Xiong, Q.; Pramanik, M.; Pu, K. Broadband Absorbing Semiconducting Polymer Nanoparticles for Photoacoustic Imaging in Second Near-Infrared Window. *Nano Lett.* **2017**, *17*, 4964-4969.

(44) Miao, Q.; Xie, C.; Zhen, X.; Lyu, Y.; Duan, H.; Liu, X.; Jokerst, J. V.; Pu, K. Molecular Afterglow Imaging with Bright, Biodegradable Polymer Nanoparticles. *Nat. Biotechnol.* **2017**, *35*, 1102.

(45) Zhu, H.; Li, J.; Qi, X.; Chen, P.; Pu, K. Oxygenic Hybrid Semiconducting Nanoparticles for Enhanced Photodynamic Therapy. *Nano Lett.* **2017**, *18*, 586-594.

(46) Chen, H.; Zhang, J.; Chang, K.; Men, X.; Fang, X.; Zhou, L.; Li, D.; Gao, D.; Yin, S.; Zhang, X.; Yuan, Z.; Wu, C. Highly Absorbing Multispectral Near-Infrared Polymer Nanoparticles from one Conjugated Backbone for Photoacoustic Imaging and Photothermal Therapy. *Biomaterials* **2017**, *144*, 42-52.

(47) Lyu, Y.; Zeng, J.; Jiang, Y.; Zhen, X.; Qiu, S.; Wang, T.; Lou, X.; Gao, M.; Pu, K. Enhancing Both Biodegradability and Efficacy of Semiconducting Polymer Nanoparticles for Photoacoustic Imaging and Photothermal Therapy. *ACS Nano* **2018**, *12*, 1801-1810.

(48) Li, J.; Xie, C.; Huang, J.; Jiang, Y.; Miao, Q.; Pu, K. Semiconducting Polymer Nanoenzymes with Photothermic Activity for Enhanced Cancer Therapy. *Angew. Chem., Int. Ed.* **2018**, *57*, 3995-3990.

(49) Lyu, Y.; Xie, C.; Chechetka, S. A.; Miyako, E.; Pu, K. Semiconducting Polymer Nanobioconjugates for Targeted Photothermal Activation of Neurons. *J. Am. Chem. Soc.* **2016**, *138*, 9049-9052.

(50) Wang, Y.; Li, S.; Zhang, P.; Bai, H.; Feng, L.; Lv, F.; Liu, L.; Wang, S. Photothermal-Responsive Conjugated Polymer Nanoparticles for Remote Control of Gene Expression in Living Cells. *Adv. Mater.* **2018**, *30*, 1705418.

(51) Miao, Q.; Yeo, D. C.; Wiraja, C.; Zhang, J.; Ning, X.; Xu, C.; Pu, K. Near-Infrared Fluorescent Molecular Probe for Sensitive Imaging of Keloid. *Angew. Chem., Int. Ed.* **2018**, *130*, 1270-1274.

(52) Rosenholm, J. M.; Peuhu, E.; Eriksson, J. E.; Sahlgren, C.; Lindén, M. Targeted Intracellular Delivery of Hydrophobic Agents Using Mesoporous Hybrid Silica Nanoparticles as Carrier Systems. *Nano Lett.* **2009**, *9*, 3308-3311.

(53) Huang, X.; El-Sayed, I. H.; Qian, W.; El-Sayed, M. A. Cancer Cell Imaging and Photothermal Therapy in the Near-Infrared Region by Using Gold Nanorods. *J. Am. Chem. Soc.* **2006**, *128*, 2115-2120.

(54) Ren, X.; Zheng, R.; Fang, X.; Wang, X.; Zhang, X.; Yang, W.; Sha, X. Red Blood Cell Membrane Camouflaged Magnetic Nanoclusters for Imaging-Guided Photothermal Therapy. *Biomaterials* **2016**, *92*, 13-24.

(55) Jiang, Q.; Luo, Z.; Men, Y.; Yang, P.; Peng, H.; Guo, R.; Tian, Y.; Pang, Z.; Yang, W. Red Blood Cell Membrane-Camouflaged Melanin Nanoparticles for Enhanced Photothermal Therapy. *Biomaterials* **2017**, *143*, 29-45.

(56) Rao, L.; Bu, L. L.; Ma, L.; Wang, W.; Liu, H.; Wan, D.; Liu, J. F.; Li, A.; Guo, S. S.; Zhang, L.; Zhang, W.-F.; Zhao, X.-Z.; Sun, Z.-J.; Liu, W. Platelet-Facilitated Photothermal Therapy of Head and Neck Squamous Cell Carcinoma. *Angew. Chem., Int. Ed.* **2018**, *130*, 998-1003.

(57) Tian, Q.; Jiang, F.; Zou, R.; Liu, Q.; Chen, Z.; Zhu, M.; Yang, S.; Wang, J.; Wang, J.; Hu, J. Hydrophilic Cu_9S_5 Nanocrystals: A Photothermal Agent with a 25.7% Heat Conversion Efficiency for Photothermal Ablation of Cancer Cells *In Vivo*. *ACS Nano* **2011**, *5*, 9761-9771.

(58) Yin, W.; Yan, L.; Yu, J.; Tian, G.; Zhou, L.; Zheng, X.; Zhang, X.; Yong, Y.; Li, J.; Gu, Z. High-Throughput Synthesis of Single-Layer MoS_2 Nanosheets as a Near-Infrared Photothermal-Triggered Drug Delivery for Effective Cancer Therapy. *ACS Nano* **2014**, *8*, 6922-6933.

(59) Gao, L.; Liu, R.; Gao, F.; Wang, Y.; Jiang, X.; Gao, X. Plasmon-Mediated Generation of Reactive Oxygen Species from Near-Infrared Light Excited Gold Nanocages for Photodynamic Therapy *In Vitro*. *ACS Nano* **2014**, *8*, 7260-7271.

(60) Lv, Y.; Liu, M.; Zhang, Y.; Wang, X.; Zhang, F.; Li, F.; Bao, W.; Wang, J.; Zhang, Y.; Wei, W.; Ma, G.; Zhao, L.; Tian, Z. Cancer Cell Membrane-Biomimetic Nanoprobes with Two-Photon Excitation and Near-Infrared Emission for Intravital Tumor Fluorescence Imaging. *ACS Nano* **2018**, *12*, 1350-1358.

(61) Kalluri, R. The Biology and Function of Fibroblasts in Cancer. *Nat. Rev. Cancer* **2016**, *16*, 582.

(62) Jiang, Y.; Li, J.; Zhen, X.; Xie, C.; Pu, K. Dual-Peak Absorbing Semiconducting Copolymer Nanoparticles for First and Second Near-Infrared Window Photothermal Therapy: A Comparative Study. *Adv. Mater.* **2018**, *30*, 1705980.

(63) Lyu, Y.; Zhen, X.; Miao, Y.; Pu, K. Reaction-Based Semiconducting Polymer Nanoprobes for Photoacoustic Imaging of Protein Sulfenic Acids. *ACS Nano* **2016**, *11*, 358-367.

(64) Zhu, H.; Fang, Y.; Miao, Q.; Qi, X.; Ding, D.; Chen, P.; Pu, K. Regulating Near-Infrared Photodynamic Properties of Semiconducting Polymer Nanotheranostics for Optimized Cancer Therapy. *ACS Nano* **2017**, *11*, 8998-9009.

TOC

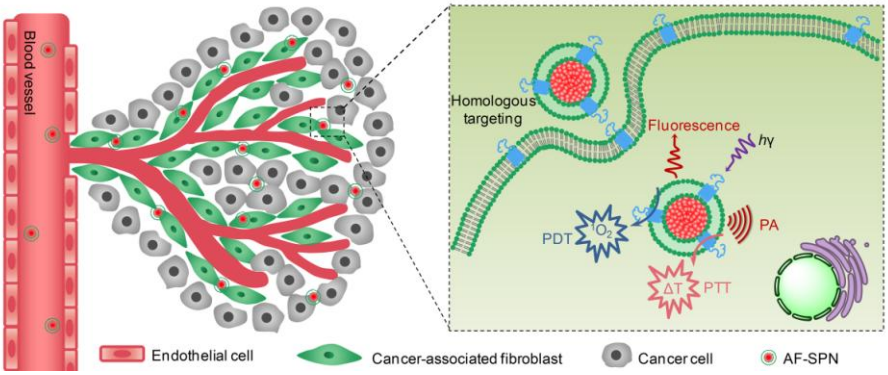
Blood vessel
Homologous targeting
Fluorescence
hγ
PDT
$^1O_2$
PA
ΔT
PTT
Endothelial cell
Cancer-associated fibroblast
Cancer cell
AF-SPN